

Measurement of Filling-Factor-Dependent Magnetophonon Resonances in Graphene Using Raman Spectroscopy

Y. Kim,¹ J. M. Poumirol,¹ A. Lombardo,² N. G. Kalugin,³ T. Georgiou,⁴ Y. J. Kim,⁴ K. S. Novoselov,⁴ A. C. Ferrari,² J. Kono,⁵ O. Kashuba,⁶ V. I. Fal'ko,^{7,8} and D. Smirnov^{1,*}

¹National High Magnetic Field Laboratory, Tallahassee, Florida 32310, USA

²Cambridge Graphene Centre, University of Cambridge, 9 JJ Thomson Avenue, Cambridge, CB3 0FA, United Kingdom

³Department of Materials and Metallurgical Engineering, New Mexico Tech, Socorro, New Mexico 87801, USA

⁴School of Physics and Astronomy, University of Manchester, Oxford Road, Manchester M13 9PL, United Kingdom

⁵Department of Electrical and Computer Engineering and Department of Physics and Astronomy, Rice University, Houston, Texas 77005, USA

⁶Institute for Theoretical Physics A, RWTH Aachen, D-52074 Aachen, Germany

⁷Department of Physics, Lancaster University, Lancaster, LA1 4YB, United Kingdom

⁸DPMC, Université de Genève, CH-1211 Genève 4, Switzerland

(Received 23 November 2012; published 29 May 2013)

We perform polarization-resolved Raman spectroscopy on graphene in magnetic fields up to 45 T. This reveals a filling-factor-dependent, multicomponent anticrossing structure of the Raman G peak, resulting from magnetophonon resonances between magnetoexcitons and E_{2g} phonons. This is explained with a model of Raman scattering taking into account the effects of spatially inhomogeneous carrier densities and strain. Random fluctuations of strain-induced pseudomagnetic fields lead to increased scattering intensity inside the anticrossing gap, consistent with the experiments.

DOI: [10.1103/PhysRevLett.110.227402](https://doi.org/10.1103/PhysRevLett.110.227402)

PACS numbers: 78.30.Na, 71.70.Di, 76.40.+b, 78.20.Bh

Magnetophonon resonances (MPRs) are observed in semiconductors when the energy of an optical phonon coincides with the inter-Landau level (LL) separation [1]. These give important information on electron-phonon interactions, especially in two-dimensional systems [2]. Electron-phonon coupling (EPC) in graphene and graphite has been investigated for several years [3–7]. The zone-center, doubly degenerate E_{2g} phonon strongly interacts with electrons, resulting in renormalization of phonon frequencies and line broadening [8–13]. These are tunable by electric and magnetic fields, through Fermi-energy shifts and Landau quantization. The Raman G peak in graphene is predicted to exhibit anticrossings when the E_{2g} phonon energy matches the separation of two LLs [14–16]. This MPR effect can be described as a resonant mixing of electronic and lattice excitations into a combined mode, leading to a splitting proportional to the EPC [15]. It was observed in magneto-Raman scattering on single layer graphene (SLG) on the surface of graphite [17,18], non-Bernal stacked multilayer graphene on SiC [19], and bulk graphite [20].

Here, we report a polarization-resolved Raman spectroscopy study of MPRs in SLG, demonstrating a strong dependence of the MPR line shape on the Raman polarization and carrier density. This is explained as a manifestation of MPRs between electronic magnetoexcitons and circularly polarized optical phonons [15], combined with the effect of inhomogeneous carrier densities and strain.

The energy spectrum of SLG in a perpendicular magnetic field B consists of discrete fourfold (spin and valley) degenerate LLs with energies $E_n = \text{sgn}(n)\sqrt{2|n|}\hbar\tilde{c}/l_B$, where $n = \dots, -2, -1, 0, 1, 2, \dots$ is the index of LLs in

the conduction ($n > 0$) and valence ($n < 0$) bands, $n = 0$ being exactly at the Dirac point (see Ref. [21] and references therein). The band velocity \tilde{c} is the slope of the Dirac cone at zero B , and $l_B = \sqrt{\hbar/eB}$ is the magnetic length. The LL occupancy is characterized by the filling factor $\nu = 2\pi l_B^2 \rho_s$, where ρ_s is the carrier density. Fully filled LLs with $n = 0, 1, \dots$ have $\nu = 2, 6, \dots$ [21]. MPRs in graphene occur when the energy of the interband inter-LL transitions $-n \rightarrow n \pm 1$ matches that of the E_{2g} phonons, resulting in strongly coupled electron-phonon modes, in which the electronic magnetoexciton is an anti-symmetric superposition of inter-LL excitations in each of the two SLG valleys, originating from the Brillouin zone points \mathbf{K} and \mathbf{K}' , while this gives symmetric superposition active in far-infrared absorption [15,22]. This effect is strongest for the E_{2g} MPR with inter-Landau-level transitions $-1 \rightarrow 0$ and $0 \rightarrow 1$ at $B_{\text{MPR}}^0 \approx 25\text{--}30$ T. Since the symmetry of such electronic excitations allows them to couple to the Raman-active E_{2g} phonons [22], MPRs manifest through a fine structure which develops in the Raman G peak in the vicinity of the MPR condition, $\Omega_{\Gamma} = [\sqrt{|n|} + \sqrt{|n| + 1}]\sqrt{2}\hbar\tilde{c}/l_B$ at B_{MPR}^n .

A specific feature of MPRs in SLG is the ν dependence of the anticrossing fine structure of coupled electron and phonon modes (which can be tuned externally by varying the carrier density), as well as a unique possibility to resolve the MPRs of circularly polarized phonons [15] (Fig. 1). The polarization properties of Raman scattering involving magnetoexcitons are such that the incoming and outgoing photons have opposite circular polarizations, with angular momentum transfer $\pm 2\hbar$, of which $\pm 3\hbar$ is

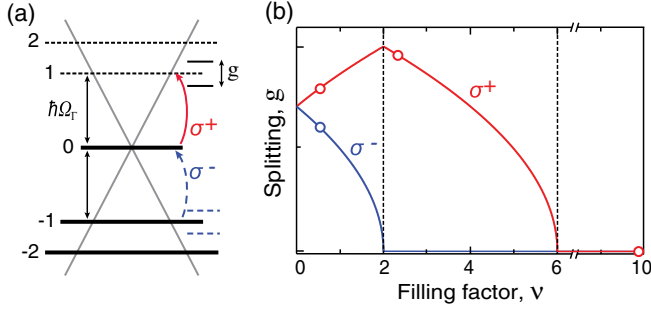


FIG. 1 (color online). (a) (grey lines) SLG band structure at $B = 0$. Mode splitting ensues in the vicinity of MPR between $0 \rightarrow 1$ electron-hole excitations and the E_{2g} phonon, for $B_{\text{MPR}}^0 \approx 25\text{--}30$ T. (b) Calculated [15] mode splitting g as a function of filling factor ν . Open circles indicate the filling factors probed in our experiment.

coherently transferred to the lattice, while the remaining angular momentum transfer $\mp \hbar$ goes into electronic excitations [22]. In the following, we will refer to this angular momentum transfer as a σ^\mp -polarized transition between the electronic LLs, with opposite signs for $-n \rightarrow n \pm 1$ inter-LL excitons: σ^+ for $-n \rightarrow n + 1$ and σ^- for $-n - 1 \rightarrow n$ valence-to-conduction band transitions. Blocking such transitions by filling (depleting) with electrons the final states, or depleting (filling) the initial states, would suppress (promote) coupling between magnetoexcitons and phonons. Since the σ^+ and σ^- magnetoexcitons are based on different LL pairs, changing carrier density in SLG would affect differently the size of the anticrossing in the MPR of σ^\mp circularly polarized phonons, as illustrated in Fig. 1. At $\nu=0$, corresponding exactly to a half-filled $n = 0$ LL, the coupling strength of σ^+ - and σ^- -polarized modes is equal, causing the G peak to split equally for σ^+ and σ^- phonon polarizations [15]. For $0 < \nu < 2$, corresponding to a more than half-filled $n = 0$ LL, the $-1 \rightarrow 0$ transition becomes partly blocked, while the $0 \rightarrow +1$ transition is promoted, giving rise to different splittings in the fine structure of σ^+ - and σ^- -polarized modes. For $2 < \nu < 6$, the $n = 0$ LL is full, leaving no space for MPRs with the σ^- phonon, whereas the $n = +1$ LL is only partly filled, resulting in a MPR-induced fine structure in the σ^+ phonon line shape (with maximum splitting at $\nu = 2$). Thus, the EPC at the MPR resolves the energies of σ^\mp -polarized lattice excitations [15,22]. Note that, in order to probe the direct B influence on the motion of lattice, nuclei would require unattainably strong $B \sim 10^4$ T or higher, as can be estimated from the carbon-atom-to-electron mass ratio. Finally, at high $\nu > 6$, both $-1 \rightarrow 0$ and $0 \rightarrow 1$ transitions are blocked, completely suppressing the MPR-induced fine structure for both modes.

We measure a SLG, grown by chemical vapor deposition on copper [23,24] and transferred onto Si/SiO₂ [25], following the procedures discussed in the Supplemental Material [26]. The carrier density is estimated by combining the intensity and area ratio of the Raman G and $2D$

peaks, $I(2D)/I(G)$ and $A(2D)/A(G)$, with the position (Pos) and full width at half maximum (FWHM) of these peaks, Pos(G), Pos($2D$), FWHM(G), and FWHM($2D$) [7,8,10]. Under ambient laboratory conditions, the SLG sample is initially p doped with a carrier concentration $\sim 5 \times 10^{12} \text{ cm}^{-2}$. By adjusting annealing parameters (typically eight hours in 90%/10% Ar/H₂ atmosphere at temperatures up to 220 °C) and degassing in $< 10^{-4}$ mbar vacuum, the sample can be made n type, with an electron density $\sim 2 \times 10^{12} \text{ cm}^{-2}$. Exposing the sample to low-pressure (~ 1 mbar or less) N_2 atmosphere reduces the carrier density to $\sim 0.4 \times 10^{12} \text{ cm}^{-2}$. The exposure to ambient pressure N_2 gas or air results in hole doping, restoring p -type doping with carrier densities $\sim 5.5 \times 10^{12} \text{ cm}^{-2}$. If the sample is left in ambient air for a long period of time, it continues to experience p doping reaching a carrier concentration $\geq 10^{13} \text{ cm}^{-2}$ in several weeks. However, this doping is inhomogeneous, with a 10%–20% variation, as shown by Raman mapping discussed in the Supplemental Material [26].

B -dependent Raman measurements are performed in a quasibackscattering configuration at 300 K for B up to 45 T, using a high-field magneto-optical insert, as for Ref. [20]. The combination of a linear polarizer and a $\lambda/4$ plate circularly polarizes the incident and scattered light. The excitation beam (532 nm) is focused to a spot $\lesssim 10 \mu\text{m}$, with a power ~ 4 mW. The circularly polarized σ^\pm excitations probed using the σ^\pm/σ^\mp configurations of out or in polarizations are achieved by reversing the B polarity. In this notation, the first (second) symbol defines the polarization of the incident (scattered) light. The polarization efficiency, i.e., the ratio of light transmitted through two circular polarizers with parallel or crossed helicities, is $\sim 90\%$ for the incident light, while it is $\sim 75\%$ for the scattered light in the spectral range of interest $\sim 1450\text{--}1700 \text{ cm}^{-1}$, as discussed in the Supplemental Material [26]. The spectral resolution is $\sim 1.9 \text{ cm}^{-1}$.

Figures 2 and 3 show the polarization and B dependence of the G peak at different carrier densities. The Raman spectra can be classified in three categories as a function of ν . At high carrier density corresponding to $|\nu| \geq 6$, the G peak does not reveal MPR-induced splitting or any polarization dependence, as seen in Figs. 2(a) and 2(b). As the filling factor decreases ($\nu < 6$), a significant change in the spectra is observed. Figures 2(c) and 2(d) plot spectra measured on the sample annealed, degassed, and kept in $< 10^{-4}$ mbar vacuum. The G peak exhibits a strong, anticrossinglike splitting, reaching $\sim 150 \text{ cm}^{-1}$ ($\sim 20 \text{ meV}$) for $B = 25$ T. The electron-phonon coupled modes appear only in the σ^+ and σ^+/σ^- geometry, while the G peak neither splits nor shifts in the σ^- and σ^-/σ^+ polarizations. This indicates n -type doping, with estimated carrier density $\sim 2.0 \times 10^{12} \text{ cm}^{-2}$. The observed behavior reveals the MPRs at $2 < \nu < 6$. Indeed, the condition $\nu = 6$ is met at $\sim B = 10$ T, with a coupling of $0 \rightarrow 1$ magnetoexcitons and E_{2g} phonons at higher B . The MPR polarization

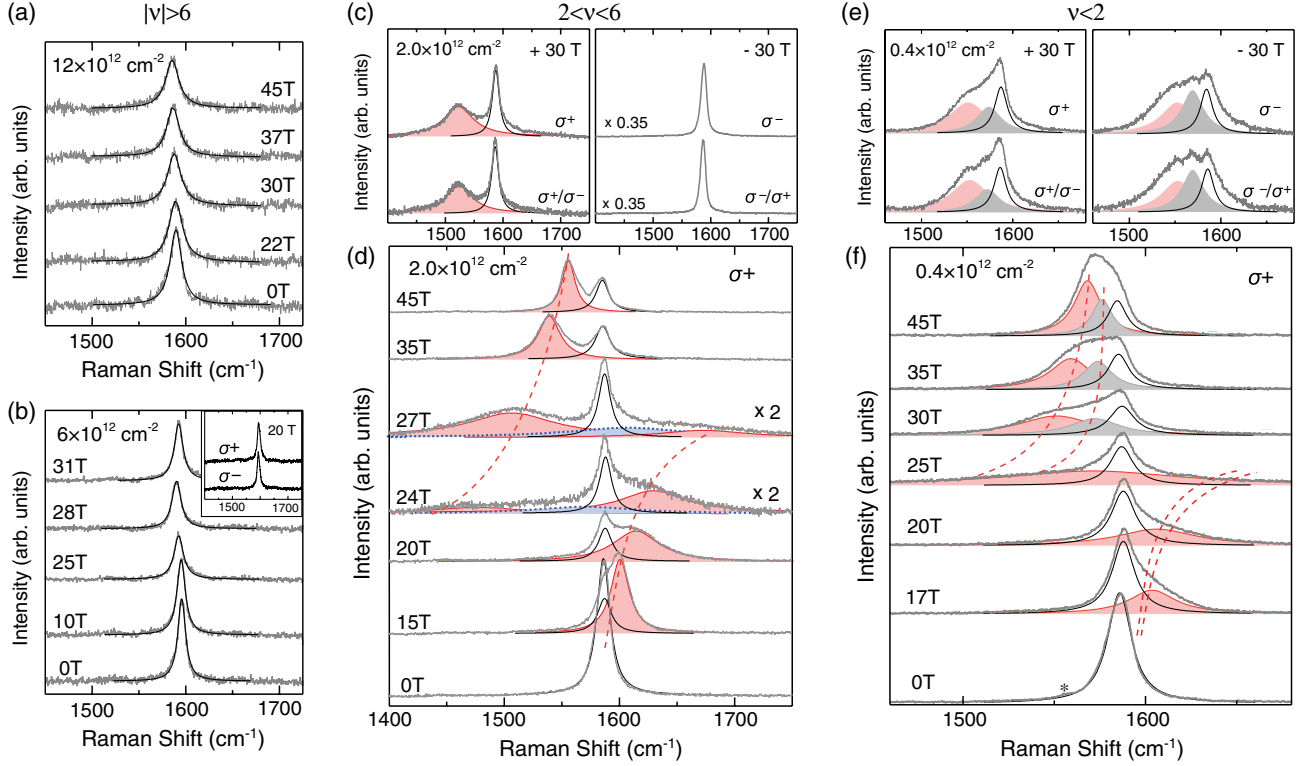


FIG. 2 (color online). (a), (b) Unpolarized magneto-Raman spectra at carrier density corresponding to $\nu \geq 6$. The inset compares 20 T σ^+ and σ^- circular polarized spectra. (c)–(f) Circular-polarized magneto-Raman spectra at (c), (d) $2 < \nu < 6$ and (e), (f) $\nu < 2$ for $B > 15$ T. (f) The star symbol points to a B -independent peak caused by parasitic scattering in fibers. This artifact, shown in the $B = 0$ spectrum, is subtracted from all other spectra. The dashed lines in (d), (f) are guides to the eye for the B dependence of electron-phonon coupled modes at the $(0 \rightarrow 1)$ MPR anticrossing. The dotted curves in (d) are additional spectral components observed in close vicinity of the intersection between the $(0 \rightarrow 1)$ magnetoexciton and the E_{2g} phonon energy.

selection rules are determined by the helicity of the incoming light only. As the carrier density further decreases, so that $\nu < 2$, the G peak splitting changes [Figs. 2(e) and 2(f)]. In contrast to the $2 < \nu < 6$ case, the coupled modes now appear in both σ^+ and σ^- polarizations. The spectra at $B \geq 30$ T reveal that the coupled mode consists of two peaks resolved in the cross-polarized measurements shown in Figs. 2(c) and 2(d) (see also the second derivative data in the Supplemental Material [26]). The relative intensities of the two MPR spectral components depend on the incoming light helicity. At 20 T, e.g., the expected separation of the two MPR components is $\sim 20 \text{ cm}^{-1}$, while their linewidths estimated from the 20 T, $2 < \nu < 6$ spectra are $\sim 50 \text{ cm}^{-1}$. We assign these two components to the σ^\pm polarized modes originating from the coupling of E_{2g} phonons with $0 \rightarrow 1$ and $-1 \rightarrow 0$ magnetoexcitons. The fact that σ^\pm polarized modes do not completely disappear in the measurements with opposite helicity is due to the imperfect polarization selectivity of our setup, combined with the presence of sample inhomogeneities, as discussed below.

For the strongest anticrossing at B_{MRP}^0 , the observed behavior can be described using the resonance approximation formula [15] for pairs of strongly coupled Ω_\pm^σ circularly polarized modes:

$$\Omega_\pm^\sigma = \frac{\Omega_\Gamma + \Omega_0}{2} \pm \sqrt{\left(\frac{\Omega_\Gamma - \Omega_0}{2}\right)^2 + \frac{g_\sigma^2}{\hbar^2}},$$

$$g_{\sigma^+}(2 < \nu < 6) = g_0 \frac{a}{l_B} \sqrt{6 - \nu}, \quad g_{\sigma^-}(2 < \nu < 6) = 0,$$

$$g_{\sigma^\pm}(0 < \nu < 2) = g_0 \frac{a}{l_B} \sqrt{2 \pm \nu}, \quad g_0 = \sqrt{\frac{3}{2}} \sqrt{\frac{\lambda_\Gamma}{4\pi}} \gamma_0. \quad (1)$$

Here, Ω_\pm^σ is the frequency of the upper (+) or lower (−) coupled mode, $\Omega_\Gamma \sim 1581 \text{ cm}^{-1}$ is the bare E_{2g} phonon frequency, $\Omega_0 = \sqrt{2} \hbar \tilde{c} / l_B$, a ($= 2.46 \text{ \AA}$) is the graphene lattice constant. g_0 describes the EPC at zero B in terms of the nearest neighbor hopping integral γ_0 and the dimensionless coupling constant λ_Γ [7,13].

The set of Eqs. (1) describes the energies of the two branches of mixed phonon and magnetoexciton modes for an idealized, nonstrained, homogeneously doped SLG, when the broadening of the bare excitations due to inelastic and elastic scattering is neglected. The detailed description of MPRs and their manifestation in the Raman spectrum of realistic samples should include broadening of the optical phonon γ_Γ and of the magnetoexciton γ_e , as well as possible inhomogeneity of doping and fluctuations of local strain. In a sample with a spatially varying carrier density,

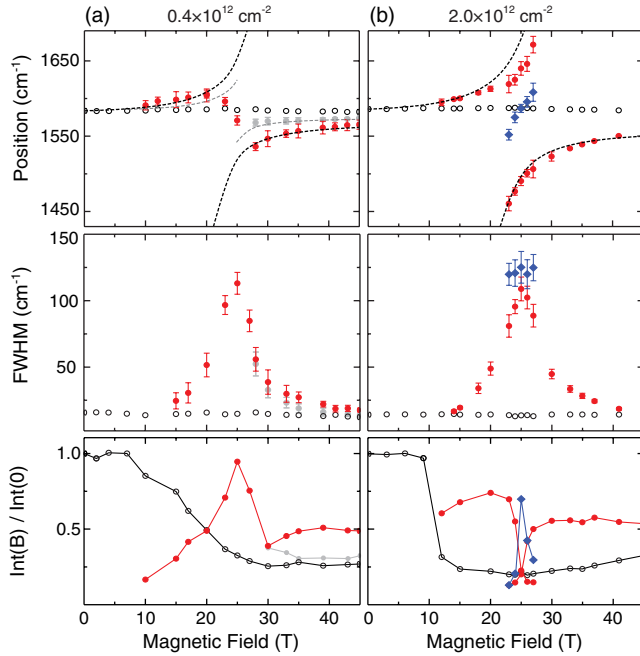


FIG. 3 (color online). Peak position, FWHM, and normalized intensity of the G peak Lorentzian components as a function of B for the (a) low and (b) intermediate carrier densities. Open black circles represent the central E_{2g} phonon line component. Filled red and grey circles are the electron-phonon coupled modes. Dashed lines plot Eq. (1). Blue squares show additional components observed close to the resonance $B_{\text{MPR}}^0 \approx 25$ T.

g^{σ^+} and g^{σ^-} become coordinate dependent, which would lead to inhomogeneous broadening of the MPR fine structure. Inhomogeneous strain in SLG generates a pseudo-magnetic field B_{str} with opposite sign in the \mathbf{K} and \mathbf{K}' valleys [5,27,28], giving a total field $B_{\mathbf{K}} = B + B_{\text{str}}$ at \mathbf{K} and $B_{\mathbf{K}'} = B - B_{\text{str}}$ at \mathbf{K}' . In strained graphene nanobubbles, it was reported that B_{str} can reach 200–400 T [29]. In nominally unstrained SLG, the residual strain caused by nm-scale height variations and defects can induce random $B_{\text{str}} > 10$ T [30]. Locally, this splits a simple anti-crossing into mixing and splitting of each σ^{\pm} -polarized phonon and two magnetoexcitons, now distinguished by different LL energies in the two valleys, leading to an even more complicated fine structure. Also, the quantum efficiency (i.e., the probability of a scattering event per incoming photon) of $0 \rightarrow 1$ and $-1 \rightarrow 0$ magnetoexcitons in Raman scattering [22] is much lower than that of the Γ optical phonon manifested in the G peak area, $A(G)$ [31].

All these factors can be taken into account in the formula for the spectral weight of Raman scattering at MPR derived using the random phase approximation [32]

$$I^{\sigma^{\pm}}(\omega) = \frac{A(G)}{2\pi} \left\langle \text{Im} \frac{1}{\omega - \Omega_G - i\gamma_{\Gamma} + \frac{\lambda_{\Gamma}}{4\pi} \sum_{\alpha} \frac{\Omega_{0,\alpha}^2}{\omega - \Omega_{0,\alpha} - i\gamma_e}} \right\rangle, \quad (2)$$

where angle brackets stand for the averaging over the spatial fluctuations of a strain-induced B_{str} , with zero

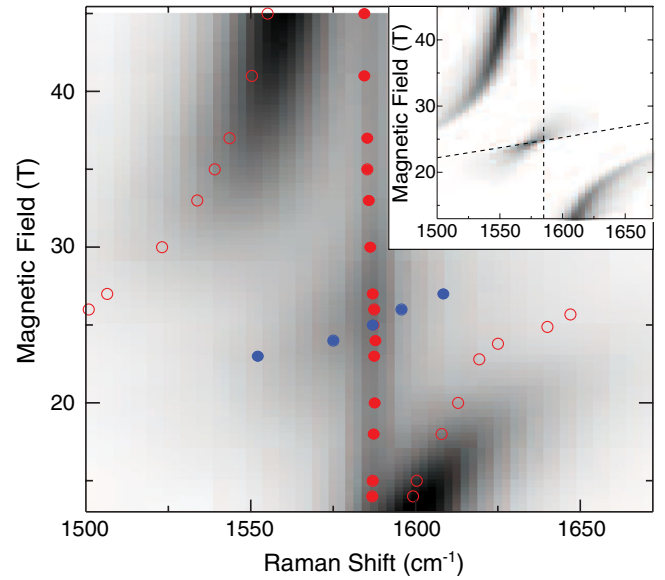


FIG. 4 (color online). MPR in SLG with $\langle \rho_s \rangle = 1.6 \times 10^{12} \text{ cm}^{-2}$ in the presence of inhomogeneous strain $\langle B_{\text{str}}^2 \rangle^{1/2} = 6$ T calculated using Eq. (2) with $\Omega_{\Gamma} \sim 1581 \text{ cm}^{-1}$, $\gamma_{\Gamma} \sim 12 \text{ cm}^{-1}$, $\gamma_e = 50 \text{ cm}^{-1}$, and $\langle \delta \rho_s^2 \rangle^{1/2} = 3 \times 10^{11} \text{ cm}^{-2}$. Symbols are experimental results. The inset shows the calculated Raman-scattering intensity neglecting LL broadening, depolarization, and inhomogeneity, but including strain-induced inhomogeneous pseudo-magnetic fields. Dashed lines indicate energies of unperturbed E_{2g} phonons and (0, 1) magnetoexcitons.

average, and over fluctuations of electron density. These together determine the local values of the inter-LL separation, $\Omega_{0,\alpha} = \sqrt{2\hbar\tilde{c}}/l_{B_{\alpha}}$ and the local filling factors of the $n = 0$ and $n = \pm 1$ LLs in each of the two valleys $\alpha = K, K'$. Equation (1), describing energies of coupled modes, can also be obtained from Eq. (2) neglecting strain and carrier density fluctuations.

To measure the EPC, we fit Eq. (1) to the data of Fig. 3. The high-field anticrossing branches (Ω_{-}) are most accurately resolved, therefore most suitable for fitting. The energy of the unperturbed electronic transition Ω_0 is calculated using $\tilde{c} = 1.08 \times 10^6$ m/s, which corresponds to the MPR at 25 T. For low carrier density ($0.4 \times 10^{12} \text{ cm}^{-2}$), we obtain $g_0^{\sigma^+} = 17 \text{ cm}^{-1}/\text{T}^{1/2}$ and $g_0^{\sigma^-} = 12 \text{ cm}^{-1}/\text{T}^{1/2}$. For intermediate carrier density ($2.0 \times 10^{12} \text{ cm}^{-2}$), fitting yields $g_0^{\sigma^+} = 21 \text{ cm}^{-1}/\text{T}^{1/2}$. Plugging the fitted $g^{\sigma^{\pm}}$ into Eq. (1), we find ν at the resonance B and extract carrier densities $\sim 0.4 \times 10^{12}$ and $\sim 1.6 \times 10^{12} \text{ cm}^{-2}$ for the low and intermediate density samples, respectively, in excellent agreement with those derived from the Raman spectra. Taken together, these results allow us to deduce λ_{Γ} . Notably, the values we obtain for the low and intermediate density samples differ by less than 5%. We get $\lambda_{\Gamma} \approx 0.028$, in remarkable agreement with that measured from FWHM(G) in undoped samples at $B = 0$, and predicted by density functional theory [3,7,13].

Finally, we discuss the observation of Raman scattering in the middle of the MPR anticrossing gap. The spectra for

intermediate carrier density show an additional component, indicated by dotted curves in Fig. 2(d). This is detected over a narrow B range, between 23 and 27 T, reaching maximum intensity at 25 T. Though we are not able to spectrally resolve this component at lower carrier density, a similar sharp increase of intensity is observed in the vicinity of the MPR at 25 T [Fig. 3(a), bottom panel]. Analysis of Eq. (2) reveals that a finite Raman scattering inside the anticrossing gap is a specific signature of MPR in strained SLG. Figure 4 plots the scattering intensity calculated for intermediate carrier densities. To model the experiment, we assume density fluctuations described by a normal distribution with average $\langle\rho_s\rangle \sim 1.6 \times 10^{12} \text{ cm}^{-2}$, and 20% standard deviation, imperfect light polarization leading to a 75%/25% mixture of σ^+ and σ^- spectra, LL and E_{2g} phonon broadening of $\gamma_e = 50 \text{ cm}^{-1}$ and $\gamma_\Gamma = 12 \text{ cm}^{-1}$, and most importantly, inhomogeneous strain, $\langle B_{\text{str}}^2 \rangle^{1/2} = 6 \text{ T}$. Away from the $\Omega_0 = \Omega_\Gamma$ MPR intersection point, the scattering intensity follows the expected anticrossing MPR behavior, while the increased scattering in the middle of the anticrossing gap is due to the overall effect of inhomogeneous strain. This is further illustrated in the inset in Fig. 4, with a scattering intensity map calculated for the ideal case of uniformly doped SLG ($\delta\rho_s = 0$) exposed to the same random B_{str} , neglecting broadening ($\gamma_\Gamma = \gamma_e = 0$) and depolarization.

In summary, we used polarization-resolved high-field magneto-Raman spectroscopy to investigate magnetophonon resonances in graphene. By varying the filling factor, we identified different types of G peak magnetic-field dependencies, providing a comprehensive experimental evidence of MPRs on circularly polarized phonons. We also detected an unexpected increase of Raman intensity in the middle of the MPR anticrossing gap and assigned it to mixing and splitting of electron-phonon coupled modes, caused by fluctuations of strain-induced pseudomagnetic fields.

We acknowledge funding from NHMFL Grant No. UCGP-5068, DOE/BES Grants No. DE-FG02-07ER46451 and No. DE-FG02-06ER46308, the Robert A. Welch Foundation Grant No. C-1509, EPSRC Grants GR/S97613/01, EP/E500935/1, EP/K01711X/1, EP/K017144/1, and EP/G042357/1, ERC Grant NANOPOTS, EU grants GENIUS and RODIN, the Leverhulme Trust, Royal Society, NSF ECCS Grant No. 0925988, ERC AdG “Graphene and Beyond.” The NHMFL is supported by the NSF Cooperative Agreement No. DMR-0654118, by the State of Florida, and by the DOE.

*smirnov@magnet.fsu.edu

- [1] V.L. Gurevich and Yu. A. Firsov, *Zh. Eksp. Teor. Fiz.* **40**, 199 (1961) [*Sov. Phys. JETP* **13**, 137 (1961)].
- [2] Yu. A. Firsov *et al.*, in *Landau Level Spectroscopy*, edited by G. Landwehr and E.I. Rashba (Elsevier, Amsterdam, 1991), p. 1192; R.J. Nicholas, *ibid.*, p. 779.
- [3] S. Piscanec, M. Lazzeri, F. Mauri, A.C. Ferrari, and J. Robertson, *Phys. Rev. Lett.* **93**, 185503 (2004).
- [4] A.C. Ferrari *et al.*, *Phys. Rev. Lett.* **97**, 187401 (2006).
- [5] T. Ando, *J. Phys. Soc. Jpn.* **75**, 124701 (2006).
- [6] A.C. Ferrari and D.M. Basko, *Nat. Nanotechnol.* **8**, 235 (2013).
- [7] D.M. Basko, S. Piscanec, and A.C. Ferrari, *Phys. Rev. B* **80**, 165413 (2009).
- [8] S. Pisana, M. Lazzeri, C. Casiraghi, K.S. Novoselov, A.K. Geim, A.C. Ferrari, and F. Mauri, *Nat. Mater.* **6**, 198 (2007).
- [9] J. Yan, Y. Zhang, P. Kim, and A. Pinczuk, *Phys. Rev. Lett.* **98**, 166802 (2007).
- [10] A. Das *et al.*, *Nat. Nanotechnol.* **3**, 210 (2008).
- [11] A. Das, B. Chakraborty, S. Piscanec, S. Pisana, A.K. Sood, and A.C. Ferrari, *Phys. Rev. B* **79**, 155417 (2009).
- [12] J. Yan, T. Villarsen, E.A. Henriksen, P. Kim, and A. Pinczuk, *Phys. Rev. B* **80**, 241417(R) (2009).
- [13] M. Lazzeri, S. Piscanec, F. Mauri, A.C. Ferrari, and J. Robertson, *Phys. Rev. B* **73**, 155426 (2006).
- [14] T. Ando, *J. Phys. Soc. Jpn.* **76**, 024712 (2007).
- [15] M.O. Goerbig, J.-N. Fuchs, K. Kechedzhi, and V.I. Falko, *Phys. Rev. Lett.* **99**, 087402 (2007).
- [16] T. Ando, *J. Phys. Soc. Jpn.* **76**, 104711 (2007).
- [17] J. Yan, S. Goler, T.D. Rhone, M. Han, R. He, P. Kim, V. Pellegrini, and A. Pinczuk, *Phys. Rev. Lett.* **105**, 227401 (2010).
- [18] C. Faugeras, M. Amado, P. Kossacki, M. Orlita, M. Kühne, A.A.L. Nicolet, Yu.I. Latyshev, and M. Potemski, *Phys. Rev. Lett.* **107**, 036807 (2011).
- [19] C. Faugeras, M. Amado, P. Kossacki, M. Orlita, M. Sprinkle, C. Berger, W.A. de Heer, and M. Potemski, *Phys. Rev. Lett.* **103**, 186803 (2009).
- [20] Y. Kim, Y. Ma, A. Imambekov, N.G. Kalugin, A. Lombardo, A.C. Ferrari, J. Kono, and D. Smirnov, *Phys. Rev. B* **85**, 121403(R) (2012).
- [21] A.H. Castro Neto, F. Guinea, N.M.R. Peres, K.S. Novoselov, and A.K. Geim, *Rev. Mod. Phys.* **81**, 109 (2009).
- [22] O. Kashuba and V.I. Fal’ko, *Phys. Rev. B* **80**, 241404 (2009).
- [23] X. Li *et al.*, *Science* **324**, 1312 (2009).
- [24] S. Bae *et al.*, *Nat. Nanotechnol.* **5**, 574 (2010).
- [25] F. Bonaccorso, A. Lombardo, T. Hasan, Z. Sun, L. Colombo, and A.C. Ferrari, *Mater. Today* **15**, 564 (2012).
- [26] See Supplemental Material at <http://link.aps.org/supplemental/10.1103/PhysRevLett.110.227402> for sample preparation and Raman characterization details.
- [27] S.V. Iordanskii and A.E. Koshelev, *JETP Lett.* **41**, 574 (1985).
- [28] A.F. Morpurgo and F. Guinea, *Phys. Rev. Lett.* **97**, 196804 (2006).
- [29] N. Levy, S.A. Burke, K.L. Meaker, M. Panlasigui, A. Zettl, F. Guinea, A.H. Castro Neto, and M.F. Crommie, *Science* **329**, 544 (2010).
- [30] N.-C. Yeh, M.-L. Teague, S. Yeom, B.L. Standley, R.T.-P. Wu, D.A. Boyd, and M.W. Bockrath, *Surf. Sci.* **605**, 1649 (2011).
- [31] D.M. Basko, *New J. Phys.* **11**, 095011 (2009).
- [32] O. Kashuba and V.I. Falko, *New J. Phys.* **14**, 105016 (2012).